

Aharonov-Bohm oscillations in phosphorene quantum rings: mass anisotropy compensation by confinement potential

Tanmay Thakur and Bartłomiej Szafran
AGH University of Science and Technology,
Faculty of Physics and Applied Computer Science,
al. Mickiewicza 30, 30-059 Kraków, Poland

We consider the Aharonov-Bohm (AB) effect on a confined electron ground state in a quantum ring defined electrostatically within the phosphorene monolayer. The strong anisotropy of effective masses in phosphorene quenches ground-state oscillations for a circular ring because of interrupted persistent current circulation around the ring. An elliptic deformation of the confinement potential can compensate for the anisotropy of the effective masses and produce ground-state parity transformations with the AB periodicity. Moreover, a specific ratio of the semiaxes is determined for which the spectrum becomes identical to that of a circular quantum ring and an isotropic effective mass. We identify a generalized angular momentum operator which commutes with the continuum Hamiltonian for the chosen ratio of the semi-axes that closes the avoided crossings of energy levels for states of the same parity and spin. Ground-state oscillations for the two-electron ground state are also discussed.

I. INTRODUCTION

Phosphorene [1] or a monolayer form of black phosphorus [2–4] is extensively studied for optics [5], field effect transistors [2, 6, 7] and quantum Hall effects [8–10]. Unlike the half-metallic graphene, phosphorene is a direct gap semiconductor that can host the electrostatic lateral confinement of electrons. The electrostatic fields produce a clean confinement in gated two-dimensional systems for investigation of the single-electron and interaction effects [11] in carriers traps. A particular form of the lateral confinement that attracts a lot of attention is the quantum ring [12]. The annular confinement allows for persistent current circulation in the presence of an external magnetic field, with the spectrum and magnetic response which is periodic with the Aharonov-Bohm periodicity [13]. The periodicity of the spectrum of a phosphorene ring defined as a rectangular flake of the crystal with a central opening has been studied in Ref. [14] including the effect of the zigzag and armchair edges of the crystal. The purpose of this paper is to investigate a clean quantum ring defined within phosphorene by an external potential that keeps the electrons off the edges of the crystal and is not affected by its details.

The anisotropy of the phosphorene crystal structure [4] results in a strongly anisotropic electron effective mass [2, 15–18] that is much larger along the zigzag chains of ions [16] than in the perpendicular direction. The anisotropy prevents the persistent current flow in the electron ground state confined in a circular ring. However, current circulation can be restored by deforming the confinement potential to an elliptic form. Then, the spectrum acquires a braided pattern of even and odd parity energy levels, which cross with the Aharonov-Bohm period. Moreover, we propose a geometry for the elliptic confinement in which a modified angular momentum operator, with one of the Cartesian coordinates rescaled, commutes with the Hamiltonian and the energy spectrum

becomes similar to the one of an electron in a circular quantum ring with isotropic effective mass. For a confined electron pair interacting with the Coulomb potential, the operator no longer commutes with the Hamiltonian, but the Aharonov-Bohm oscillations of the ground-state energy appear for a tuned confinement potential.

II. THEORY

A. Tight-binding model

We work with the phosphorene monolayer (see Fig. 1) using the Hamiltonian,

$$H_{TB} = \sum_{kl} t_{kl} p_{kl} c_k^\dagger c_l + \sum_k V_k c_k^\dagger c_k + g\mu_B B \sigma_z / 2, \quad (1)$$

where the first sum describes the hopping between the neighboring atoms. The values for t_{kl} (see Table I) are taken from the five-parameter effective tight-binding Hamiltonian of Ref. [17]. The positions of the ions in the phosphorene crystal [3] are plotted in Fig. 1 with the zigzag chains oriented along the y direction. In Eq. (1), p_{kl} are the Peierls phase shifts that the electron acquires from the vector potential along the line between k and l ions, $p_{kl} = e^{i\frac{e}{\hbar} \int_{r_k}^{r_l} \vec{A} \cdot d\vec{l}}$. We consider the magnetic field perpendicular to the monolayer $(0, 0, B)$ with the vector potential taken in the symmetric gauge $\mathbf{A} = (-\frac{By}{2}, \frac{Bx}{2}, 0)$. In Eq. (1), V_k stands for the external potential on the ion k . The spin Zeeman effect is introduced by the last term of the Hamiltonian.

The g -factor for phosphorene of $g \approx 2.03$ was determined using $\mathbf{k} \cdot \mathbf{p}$ theory by Junior *et al.* [19]. Zhou *et al.* [20] indicated the value of $g = 2.14$ for monolayer black phosphorus. On the other hand, experiments have determined the value of $g = 2 \pm 0.1$ [21] and $g \approx 1.8 - 2.7$ [22] and some have even reported $g = 5.7 \pm 0.7$ at low filling

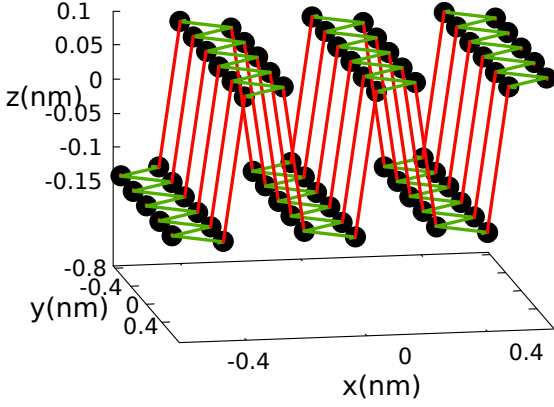


FIG. 1. Ions in phosphorene monolayer placed on two planes separated by a distance of 0.213 nm. The lines link the neighbor ions with the largest hopping energies (in-plane neighbors, green lines, hopping energy -1.22 eV) and (neighbors of separate planes, red lines, hopping energy 3.665 eV), see Table I.

$r_{kl}(\text{nm})$	$t_{kl}(\text{eV})$
0.222	-1.22
0.224	3.665
0.334	-0.205
0.347	-0.105
0.423	-0.055

TABLE I. Hopping energies according to Ref. [17] for a single black phosphorus layer. The left column shows the distance between the ions and the right column the hopping energy t_{kl} applied in the tight-binding Hamiltonian (1).

factors. Nevertheless, the spin Zeeman term produces only a linear shift in the energy defining the spin splitting. The magnetic field promotes the spin-down energy levels to the ground state sooner or later on the magnetic field scale. We focus on avoided crossings or crossings of the states of the polarized spin. The absence or presence of Aharonov-Bohm oscillations will not be affected by the value of the g -factor. Therefore, the spin Zeeman term is calculated with the value $g = 2$.

B. Effective-mass Hamiltonian

Part of the results of this work is obtained in the continuum approximation to the tight-binding Hamiltonian. We use a single-band effective-mass operator,

$$H_{em} = \left(-i\hbar \frac{\partial}{\partial x} + eA_x \right)^2 / 2m_x + \left(-i\hbar \frac{\partial}{\partial y} + eA_y \right)^2 / 2m_y + V(x, y) + g\mu_B B \sigma_z / 2. \quad (2)$$

with the effective mass parameters derived by fitting the tight-binding spectrum to the harmonic oscillator spectrum in Ref. [24] with mass about five times heavier for the carrier motion along the zigzag chains of the crystal

(see Fig. 1), $m_x = 0.17037m_0$ and $m_y = 0.85327m_0$. The effective mass Hamiltonian is diagonalized using the finite-difference technique.

C. Confinement potential

We attempt to compensate for the anisotropy of the effective masses by the anisotropy of the confinement potential. For that purpose, we use the following external potential

$$V(x, y) = \frac{1}{2} m_x \omega^2 (\rho(x, y) - R)^2, \quad (3)$$

with $\rho(x, y) = \sqrt{x^2 + y^2/\alpha}$, where α is a parameter that controls the anisotropy of the potential. The potential vanishes for points (x, y) forming an ellipse

$$\frac{x^2}{R^2} + \frac{y^2}{\alpha R^2} = 1. \quad (4)$$

We take the confinement energy $\hbar\omega = 6$ meV. Changing α we keep the area within the ellipse fixed taking $R = \alpha^{-1/4} R_c$, with $R_c = 30$ nm, so that the number of magnetic flux quanta threading the ellipse is the same for a given magnetic field B independent of α . For $R_c = 30$ nm a flux quantum threads the ring at 1.43 T, which is the period of the energy spectrum on the B scale for a strictly 1D circular quantum ring. We use $\alpha \leq 1$ so that the half length of the major axis a of the ellipse is oriented along the x axis $a = R = \alpha^{-1/4} R_c$ and the half length of the minor axis is $b = \sqrt{\alpha} R = \alpha^{1/4} R_c$.

In this work, we focus on the confined electron states of the conduction band. In the continuum Hamiltonian, the bottom of the conduction band is set as the reference energy level. The tight-binding spectrum produces the conduction and valence bands extrema spaced by the energy gap. For a finite flake, the spectrum contains also in-gap states that are localized at the edge of the flake and the spectrum is not symmetric with respect to the center of the energy gap [14]. Ref. [14] which used the same tight-binding parameterization [17] provides the lowest conduction-band state energy level of $\simeq 0.4$ eV for a square flake with a side length of 8 nm in the absence of external potential. In this paper, we are interested in states confined in the external potential that are independent of the details of the edge and thus correspond to an infinite crystal. However, the calculations are carried out in an elliptical flake for which the position of the ions satisfies the condition $x^2 + y^2/\alpha < R_s^2$. We take the flake large enough to contain all the discussed states within the confinement potential so that the results are independent of R_s . However, for $V = 0$, the conduction band states occupy the entire flake, and the results depend on R_s [25]. The dependence on the lowest energy level in R_s is well approximated by the dependence $E_0(R_s) = C/R_s^2 + E_\infty$, where $C = 673.31(\text{meV nm}^2)$ and $E_\infty = 340$ meV. The R_s^{-2} dependence is due to the finite-size effect, that is,

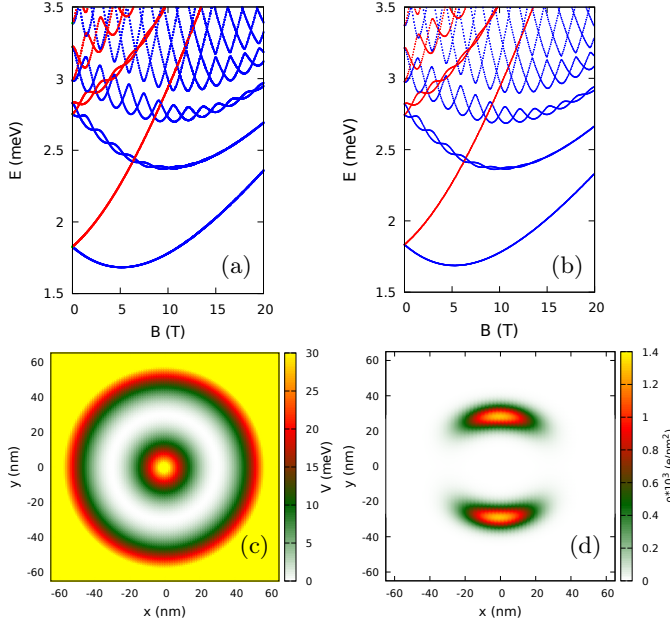


FIG. 2. The tight binding (a) and continuum Hamiltonian (b) eigenvalues for $\alpha = 1$. The blue and red lines show the spin-down and spin-up energy levels respectively. The tight-binding energy levels in (a) were shifted down by $E_\infty = 340$ meV (see text in II.B). Panel (c) show the confinement potential and panel (d) the ground-state charge density for $B = 0$ calculated using the continuum model.

the kinetic energy due to localization in a finite flake, and $E_\infty = 340$ meV is the estimated position of the bottom of the conduction band for an infinite crystal. In the results presented in the following we shift down the tight-binding energies by E_∞ .

III. RESULTS AND DISCUSSION

A. Single-electron solutions

The low-energy spectrum of a circular ring ($\alpha = 1$) is plotted in Fig. 2(a) (Fig. 2(b)) for the tight-binding model (continuum model). The TB results [Fig. 2(a)] here and below are shifted down by 340 meV. The results of both approaches are nearly identical. The ground state of a circular ring is localized in two islands near the y axis on the opposite sides of the ring center [Fig. 2(c)]. The variation of the wave function implies a contribution to the kinetic energy which is large on the $x = 0$ axis due to the low value of mass m_x . In consequence the ground-state wave function is far from the x axis, and no persistent current circulation is possible in the ground-state.

The lowest spin-up and spin-down energy levels of Fig. 2(a,b) are two-fold degenerate with respect to the parity. Degeneracy results from the lack of tunnelling of the wave function across the x axis (Fig. 2(d)). In the excited state

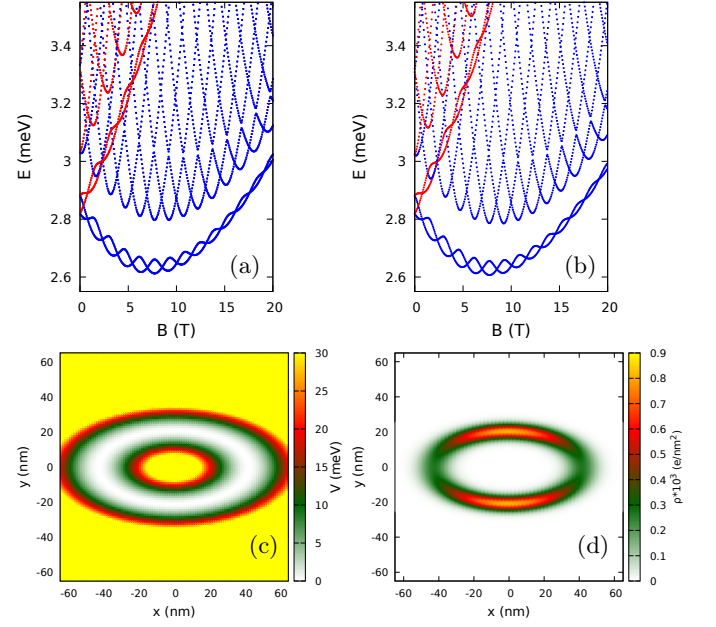


FIG. 3. Same as Fig. 2 only for $\alpha = 1.2 \frac{m_x}{m_y}$.

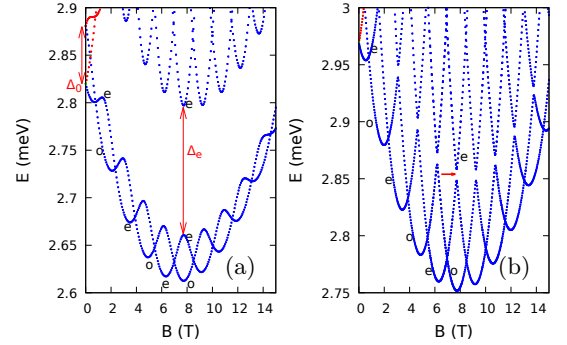


FIG. 4. Magnified view of the low-energy part of the tight-binding spectrum for $\alpha = 1.2 \frac{m_x}{m_y}$ (a) [Fig. 4(a)] and $\alpha = \frac{m_x}{m_y}$ (b) [Fig. 6(a)]. Letters 'e' and 'o' near the energy levels in (a) mark the even and odd parity energy levels that are eigenstates of the parity operator with the eigenvalues $+1$ and -1 , respectively. Δ_0 is the even-odd parity splitting at $B = 0$ and Δ_e is the width of the avoided crossing between the lowest even parity energy levels for $B \simeq 7.75$ T. The red arrow in (b) shows the avoided crossing Δ_e , here of the width of $13\mu\text{eV}$. (see Table II).

part of the spectrum, one can see pairs of energy levels that cross in a braid-like pattern. The corresponding states have opposite parities, hence the crossings of the levels. These oscillations are reminiscent of the angular momentum transitions for a circular ring with isotropic effective mass [12, 26].

With $\alpha < 1$ the confinement area on the y axis becomes thinner and the one along the x axis wider [see Fig. 3(c) for $\alpha = 1.2 \frac{m_x}{m_y}$]. The confinement energy along the y -axis increases and that along the x -axis decreases. The x axis is now accessible for the ground-state electron [Fig.

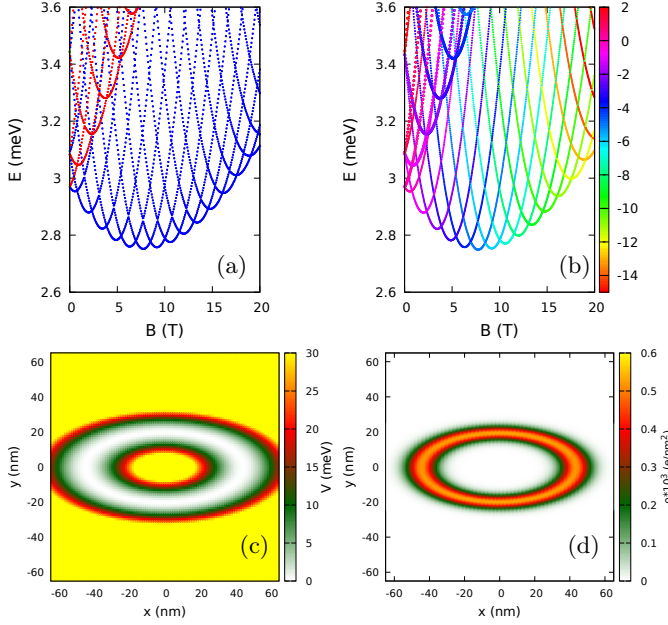


FIG. 5. Same as Fig. 2 only for $\alpha = \frac{m_x}{m_y}$. In panel (b) the colors indicate the eigenvalue of the angular momentum l'_z operator, and in panel (a) the colors describe the spin as in Fig. 2.

3(d)]. The ground-state degeneracy is lifted, and the ground-state crossings of energy levels of opposite parity are observed [Fig. 3(a,b)].

In Fig. 4(a) we plotted a magnified view of the low-energy part of the spectrum. By Δ_0 we denote the energy splitting of the lowest even and odd parity energy levels taken at $B = 0$, which defines the range of the ground-state energy oscillations as functions in the external magnetic field. The braided two energy levels cross with the Aharonov-Bohm period. The second quantity marked in Fig. 4(a) by Δ_e is the width of the avoided crossing of even-parity energy levels taken at $B \simeq 7.75$ T.

Decreasing the anisotropy parameter to $\alpha = \frac{m_x}{m_y}$ we find that the ground-state charge density [Fig. 5(d)] is constant along the confinement potential minimum Fig. 5(c)]. The continuum spectrum [Fig. 5(b)] contains crossings of energy levels in the entire spectrum. For the tight-binding model – see also Fig. 4(b) – we find the parity-related crossings of the energy levels in the ground state as in Fig. 3, and only narrow avoided crossings are found between the first and second excited energy levels of the same parity. The one marked by the red arrow in Fig. 4(b) corresponds to $\Delta_e = 13$ μeV . Δ_e attains its minimal value for $\alpha = \frac{m_x}{m_y}$. Values of Δ_0 and Δ_e calculated with the tight binding approach for varied α are summarized in Table II.

α	$\alpha/(m_x/m_y)$	Δ_0 (meV)	Δ_e (meV)
1	2.238	0.001	0.673
0.894	2	0.012	0.414
0.536	1.2	0.061	0.137
0.469	1.05	0.096	0.046
0.447	1	0.113	0.013
0.424	0.95	0.104	0.028

TABLE II. The spacing Δ_0 between the lowest energy levels of even and odd parity for $B = 0$ (see Fig. 4(a)) and the Δ_e width of the avoided crossing between the two lowest energy levels of even parity (Fig. 4(a)) as a function of the eccentricity parameter α for $B \simeq 7.75$ T. The results are calculated with the tight binding approach.

B. Angular momentum in the rescaled space

The crossings of the energy levels in the spectrum of Fig. 5(b) suggest that an additional symmetry is present in addition to the parity. With the substitution $y' = y/\sqrt{\alpha}$ and $\alpha = \frac{m_x}{m_y}$ the Hamiltonian (2) becomes

$$H_{em} = -\frac{\hbar^2}{2m_x} \left(\frac{\partial^2}{\partial x^2} + \frac{\partial^2}{\partial y'^2} \right) + \frac{e^2 B^2}{8m_y} (x^2 + y'^2) + \frac{eB}{2\sqrt{m_x m_y}} l'_z + V(\rho' - R) + g\mu_B B \sigma_z / 2, \quad (5)$$

with $\rho' = \sqrt{x^2 + y'^2}$ and the z component angular momentum operator in the deformed space $l'_z = i\hbar \left(y' \frac{\partial}{\partial x} - x \frac{\partial}{\partial y'} \right)$. The confinement potential acquires circular symmetry upon rescaling of the y coordinate and the Hamiltonian commutes with l'_z operator. The crossings of the eigenstates of the effective mass Hamiltonian are due to the symmetry which upon rescaling of the y coordinate is no longer hidden. The l'_z eigenvalues are given by color in Fig. 5(b). The ground state undergoes l'_z angular momentum transitions similar to the ones found for circular quantum rings with isotropic electron effective mass [26]. Note that the applicability of l'_z operator is not limited to quantum rings, but it can also be used to any potential profile which is radially symmetric for the rescaled y coordinate.

C. 1D limit

For a narrow radial confinement (large ω) the low-energy part of the spectrum occupy the same state of radial quantization and there is essentially one degree of freedom of motion along the ring. The Hamiltonian (5) put in circular coordinates reads

$$H_{em} = -\frac{\hbar^2}{2m_x} \left(\frac{1}{\rho'} \frac{\partial}{\partial \rho'} + \frac{\partial^2}{\partial \rho'^2} - \frac{l_z'^2}{\rho'^2} \right) + \frac{B}{2\sqrt{m_x m_y}} l'_z + \frac{e^2 B^2}{8m_y} \rho'^2 + V(\rho' - R), \quad (6)$$

where we neglected the spin Zeeman term. For strong confinement (large ω) the radial profile of the wave function no longer depends on l'_z or B . Then, the terms with the derivatives with respect to ρ' and the external potential produce the same energy contribution for all the states involved. With this contribution set as the reference energy level, we obtain the energy spectrum of the form,

$$E(l'_z, B) = \frac{\hbar^2 l_z'^2}{2m_x R^2} + \frac{e^2 B^2}{8m_y} R^2 + \frac{eB}{2\mu} l'_z, \quad (7)$$

where $\mu = \sqrt{m_x m_y}$. With $R = \left(\frac{m_y}{m_x}\right)^{1/4} R_c$ one obtains an expression that is symmetric in the effective masses,

$$\begin{aligned} E(l'_z, B) &= \frac{\hbar^2 l_z'^2}{2\mu R_c^2} + \frac{e^2 B^2}{8\mu} R_c^2 + \frac{eB}{2\mu} l'_z \\ &= \frac{\hbar^2}{2\mu R_c^2} \left(\frac{\Phi}{\Phi_0} + l'_z \right)^2, \end{aligned} \quad (8)$$

where $\Phi_0 = \frac{h}{e} = \frac{2\pi\hbar}{e}$ is the flux quantum and $\Phi = B\pi R_c^2$. The final result with the geometric average of the effective masses is identical to that of the circular ring with an isotropic effective mass [26].

Figure 6 shows the 2D continuum Hamiltonian (6) spectra with the spin Zeeman effect excluded for $\hbar\omega = 6$ meV in Fig. 6(a), $\hbar\omega = 120$ meV in Fig. 6(b) and the results of the 1D formula in Fig. 6(c). In Fig. 6(a) we see a diamagnetic shift of the spectrum to higher energy. The period of the Aharonov-Bohm oscillations is slightly larger than in the 1D results due to compression of the wave function by the external magnetic field that decreases average ρ' below R_c . For the radial wave function confined stronger around R_c in Fig. 6(b), we see the results approach the results for the analytical formula (8).

D. Two-electron spectrum

The electron-electron interaction potential does not commute with the l'_z operator, so the presence of the ground-state oscillations is not given a priori. We calculated the two-electron energy spectrum in the continuum approach using the Hamiltonian

$$H_{2e} = H_{em}(\mathbf{r}_1) + H_{em}(\mathbf{r}_2) + \frac{e^2}{4\pi\epsilon_0\epsilon} \frac{1}{r_{12}}, \quad (9)$$

where H_{em} is the single-electron Hamiltonian (2), and $\epsilon = 12$ is taken. The two-electron Hamiltonian is diagonalized in the basis of up of the two-electron Slater determinants constructed from the 30 lowest-energy single-electron eigenfunctions of Hamiltonian (2).

For both $\alpha = 1$ (Fig. 7(a)) and $\alpha = \frac{m_x}{m_y}$ (Fig. 7(c)) at $B = 0$ the ground state is four-fold degenerate, with singlet and triplet energy levels of the same energy. The exchange interaction is zero since the electrons form single-electron islands that are completely separated. For $\alpha = 1$

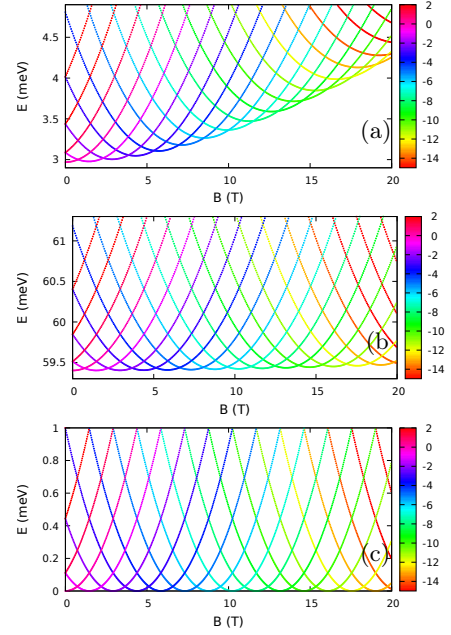


FIG. 6. The energy spectrum of Hamiltonian (5) with $g = 0$ for $\hbar\omega = 6$ meV (a), $\hbar\omega = 120$ meV (b), and the 1D formula (7). The color of the lines gives the l'_z operator eigenvalue

the localization of the charge density formed a single-electron island already without interaction (Fig. 2(d)). For $\alpha = \frac{m_x}{m_y}$ the electron-electron interaction separates the electron density to the opposite ends of the longer semiaxis of the ellipse (Fig. 7(d)). A more or less uniform electron distribution is obtained for $\alpha = 1.7 \frac{m_x}{m_y}$ (Fig. 7(f)). In this case, the ground state for $B = 0$ is a singlet which is not degenerate with the triplet. The field of about 0.5 T promotes the triplet to the ground state. Periodic avoided crossings are observed in the ground state, which are similar to the ones found for a system with isotropic effective mass but in an anisotropic quantum ring [28]. For the circular ring, the triplet-energy levels correspond to odd values of the total angular momentum (L) [29] that correspond to the negative parity $(-1)^L$. In our two-electron system, only the parity is a good quantum number. In Fig. 7(e) we see a series of avoided crossings between the ground state and the first excited state. The avoided crossings obtained for the spin-polarized two-electron levels are observed due to the same – odd – parity of these levels, which is in contrast to the single-electron ground state where the crossings of energy levels corresponding to opposite parity were observed in the ground state.

E. Discussion

The spectra of confined quantum rings are experimentally studied for annular-shaped traps defined in gated two-dimensional electron gas [30]. The current trans-

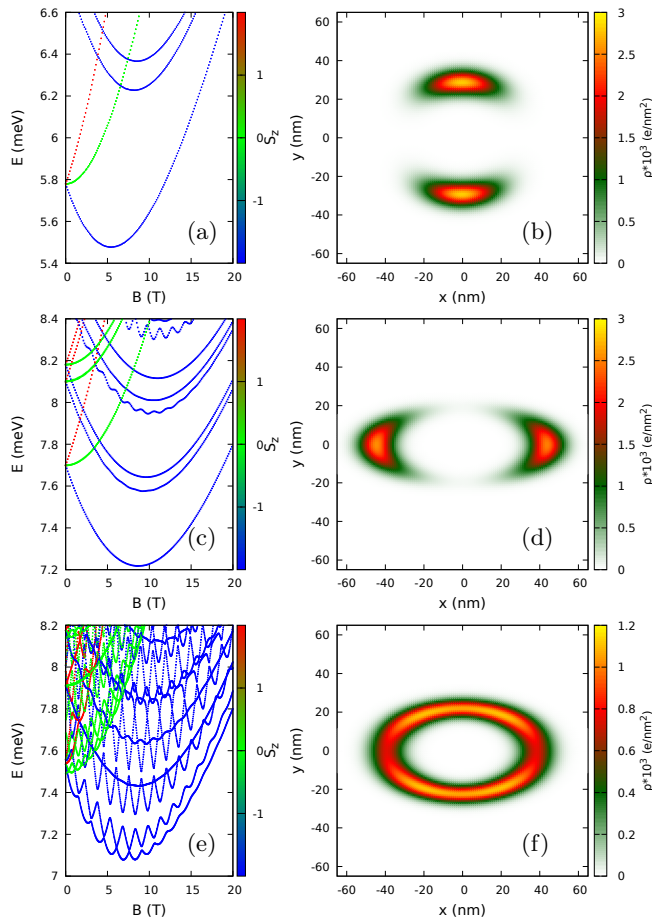


FIG. 7. The two-electron energy spectrum (a,c,e) and the ground-state charge density (b,d,f) calculated using continuum model for $B = 0$ and $\alpha = 1$ (a,b), $\alpha = \frac{m_x}{m_y}$ (c,d) and for $\alpha = 1.7 \frac{m_x}{m_y}$ (e,f). In (a,c,e) the color of the lines corresponds to the z component of the total spin.

port for electron traps weakly coupled to the electron reservoirs is governed by the Coulomb blockade [11, 31], with the single-electron current passing through the system only when the chemical potential of the confined N -electron system falls within the transport window defined by the Fermi levels of the source and drain. The technique can also be used for detection of the excited part of the spectra when the corresponding energy level enters the transport window [30, 31]. The transport spectroscopy allows for reconstruction of the energy spectra with a precision of the order of a few μeV [30] with the Aharonov-Bohm periodicity as the signature of the angular confinement. The gated quantum rings can exhibit an elliptically deformed confinement potential as in Ref. [30] in particular.

The gating techniques for phosphorene have been developed [32–34] and applied for fabrication of the field-effect transistors. The ring-like potential can be defined electrostatically in a plane plate capacitor system with a tubular electrode protruding from one of the plate elec-

trodes with the phosphorene layer embedded in a dielectric [35, 36]. For a similar gating system defined for electrons on liquid helium surface, see e.g. Ref. [27].

The results of this paper indicate the way to observe the Aharonov-Bohm effect for the system confined by the external potential in phosphorene. For circular quantum rings the Aharonov-Bohm oscillations can only be observed in the excited part of the spectrum since in the degenerate ground state the electron density forms separated islands and the persistent current circulation is interrupted. For an elliptical deformation of the confinement potential, the oscillations of the ground-state parity appear with the Aharonov-Bohm periodicity. The amplitude of these oscillations has been determined (see Δ_0 in Table II). Based on results of Ref. [30] one can expect that for $\alpha \leq 1.2 \frac{m_x}{m_y}$ the ground-state oscillation should enter the experimental resolution.

For a specifically chosen eccentricity parameter α one can reduce the spectra to those that are characteristic to a circular quantum ring with an isotropic effective mass. We explained this effect analytically in the effective mass approximation that indicates an additional symmetry found for a value of α and the spectra that agree with the tight-binding ones up to an avoided crossing in the excited energy spectra found in the latter, which is minimal for the optimal value of $\alpha = \frac{m_x}{m_y}$ (see Δ_e in Table II). The width of the avoided crossing should also be accessible for an experimental study.

IV. SUMMARY AND CONCLUSIONS

We have studied the ground-state energy oscillations in a quantum ring potential defined within monolayer black phosphorus with the tight-binding and effective mass models. In a circular quantum ring, the strong anisotropy of the effective mass produces a ground state localized along the axis related to the heavier mass. The current circulation around is possible for an elliptic ring. A braided pattern of even and odd-parity energy levels is then observed in the ground state with crossings appearing with the Aharonov-Bohm periodicity. In particular, for the ellipse with the ratio of the semiaxes equal to the effective masses ratio, the electron density becomes uniform along the ring. Then, the single-electron energy spectrum becomes similar to that of a circular quantum ring with an isotropic effective mass equal to the geometric average of the effective masses along the two crystal directions. We demonstrated that the angular momentum in the rescaled space l'_z is definite in the single-electron Hamiltonian eigenstates. We provided an analytical formula for the spectrum in the 1D limit. The applicability of the l'_z operator exceeds the quantum rings and can be used for modeling other confined systems in phosphorene. For two electrons, an elliptical deformation of the ring produces avoided crossings in the ground-state due to the same parity of low-energy spin-polarized states appearing periodically on the magnetic field scale.

ACKNOWLEDGMENTS

This work was supported by the National Science Centre (NCN) according to decision DEC-

2019/35/O/ST3/00097. Calculations were performed on the PLGrid infrastructure.

-
- [1] H. Liu, A.T. Neal, Z.Zhu, Z. Luo, X. Xu, D. Tomanek, and P.D. Ye, ACS Nano **8**, 4033 (2014).
 - [2] L. Li, Y. Yu, G. J. Ye, Q. Ge, X. Ou, H. Wu, D. Feng, X. H. Chen, and Y. Zhang, Nat. Nanotechnol. **9**, 372 (2014).
 - [3] S. Fukuoka, T. Taen, and T. Osada, J. Phys. Soc. Jpn. **84**, 121004 (2015).
 - [4] M. Akhar, G. Anderson, R.Zhao, A. Alruqi, J.E. Mroczkowska, G. Sumanasekera, J.B. Jasinski, npj 2D Mater Appl **1**, 5 (2017).
 - [5] G. Zhang, S. Huang, F. Wang, and H. Yan, Laser Photonics Rev. **15**, 2000399 (2021).
 - [6] D. He, Y. Wang, Y. Huang, Y. Shi, X. Wang, and X. Duan, Nano Lett. **19**, 331 (2019).
 - [7] X.Li, Z. Yu, X. Xiong, T. Li, T. Gao, R. Wang, R. Huang, and Yanqing Wu, Sci. Adv. **5** eaau3194 (2019).
 - [8] G. Long, D. Maryenko, J. Shen, S. Xu, J. Hou, Z. Wu, W.K. Wong, T. Han, J. Lin, Y. Cai, R. Lortz, and N. Wang, Nano Lett. **16**, 7768 (2016).
 - [9] G. Long, D. Maryenko, S. Pezzini, S. Xu, Z. Wu, T. Han, J. Lin, C. Cheng, Y. Cai, U. Zeitler, and N. Wang, Phys. Rev. B **96**, 155448 (2017).
 - [10] J. Yang, S. Tran, J. Wu, S. Che, P. Stepanov, T. Taniguchi, K. Watanabe, H. Baek, D. Smirnov, R. Chen, and C. N. Lau, Nano Lett. **18**, 229 (2018).
 - [11] R. Hanson, L. P. Kouwenhoven, J. R. Petta, S. Tarucha, and L. M. K. Vandersypen, Rev. Mod. Phys. **79**, 1217 (2007).
 - [12] V.M. Fomin, *Physics of Quantum Rings*, Springer Nature, Cham (2018).
 - [13] Y. Aharonov and D. Bohm, Phys. Rev. **115**, 485 (1959).
 - [14] L.L. Li, D. Moldovan, P. Vasilopoulos, and F. M. Peeters, Phys. Rev. B **95**, 205426 (2017).
 - [15] R. Schuster, J. Trinckauf, C. Habenicht, M. Knupfer, and B. Büchner, Phys. Rev. Lett. **115**, 026404 (2015).
 - [16] J. Qiao, X. Kong, Z.X. Hu, F. Yang, W. Ji, Nat. Commun. **5**, 4475 (2014).
 - [17] A. N. Rudenko and M. I. Katsnelson, Phys. Rev. B **89**, 201408(R) (2014).
 - [18] A. N. Rudenko, S. Yuan and M. I. Katsnelson, Phys. Rev. B **92**, 085419(R) (2015).
 - [19] P. Faria Junior, M. Kurpas, M. Gmitra, and J. Fabian, Phys. Rev. B **100**, 115203 (2019).
 - [20] X. Zhou, , W.K. Lou, D. Zhang, F. Cheng, G. Zhou, and Chang, K. Phys. Rev. B **95**, 045408 (2017).
 - [21] L. Li, F.Yang, G.J. Ye, Z. Zhang, Z. Zhu, W. Lou, X. Zhou, L. Li, K. Watanabe, T. Taniguchi, and K. Chang, Nat. Nano. **11**, 593–597 (2016).
 - [22] N. Gillgren, D. Wickramaratne, Y. Shi, T. Espiritu, J. Yang, J. Hu, J. Wei, X. Liu, Z. Mao, K. Watanabe, and T. Taniguchi, 2D Materials **2**, 011001 (2014).
 - [23] F. Yang, Z. Zhang, N.Z. Wang, G.J. Ye, W. Lou, X. Zhou, K. Watanabe, T. Taniguchi, K. Chang, X.H. Chen, and Y. Zhang, Nano Letters, **18**, 6611 (2018).
 - [24] B. Szafran, Phys. Rev. B **101**, 235313 (2020).
 - [25] With $\alpha = \frac{m_x}{m_y}$ for $R_s=25, 30, 35, \dots, 70$ (in nm) we obtain the lowest conduction band energy level at 341.066, 340.764, 340.559, 340.415, 340.328, 340.266, 340.184, 340.161, and 340.138 (in meV), respectively.
 - [26] S. Viefers, P. Koskinen, P.S. Deo, and M. Manninen, Physica E, **21** 1 (2004).
 - [27] B. Szafran, Phys. Rev. B **104**, 235402 (2021).
 - [28] V. M. Fomin, V. N. Gladilin, J. T. Devreese, N. A. J. M. Kleemans, and P. M. Koenraad, Phys. Rev. B **77**, 205326 (2008).
 - [29] J.-L. Zhu, Z. Dai, and X. Hu, Phys. Rev. B **68**, 045324 (2003).
 - [30] A. Fuhrer, S. Luescher, T. Ihn, T. Heinzel, K. Ensslin, W. Wegscheider, and M. Bichler, Nature **413**, 822 (2001).
 - [31] Kouwenhoven L.P., Marcus C.M., McEuen P.L., Tarucha S., Westervelt R.M., Wingreen N.S. (1997) Electron Transport in Quantum Dots. In: Sohn L.L., Kouwenhoven L.P., Schön G. (eds) Mesoscopic Electron Transport. NATO ASI Series (Series E: Applied Sciences), vol **345**. Springer, Dordrecht.
 - [32] L. Li, Y. Yu, Q. Ge, X. Ou, H. Wu, D. Feng, X. H. Chen, and Y. Zhang, Nat. Nanotechnol. **9**, 372 (2014).
 - [33] D. He, Y. Wang, Y. Huang, Y. Shi, X. Wang, and X. Duan, Nano Lett. **19**, 331 (2019).
 - [34] X. Li, Z. Yu, X. Xiong, T. Li, T. Gao, R. Wang, R. Huang, and Y. Wu, Sci. Adv. **5**, eaau3194 (2019).
 - [35] W. Dickerson, V. Tayari, I. Fakih, A. Korinek, M. Caporali, M. Serrano-Ruiz, M. Peruzzini, S. Heun, G. A. Botton, and T. Szkopek, App. Phys. Lett. **112**, 173101 (2018).
 - [36] B. Deng, V. Tran, Y. Xie, H. Jiang, L. Cheng, Q. Guo, X. Wang, H. Tian, S.J. Koester, H. Wang, J.J. Cha, Q. Xia, L. Yang, and F. Xia, Nat. Commun. **8**, 14474 (2017).